JOURNAL OF GEOPHYSICAL RESEARCH, VOL. 115, A07210, doi:10.1029/2009JA014949, 2010

Click Here for Full Article

Quantification of the precipitation loss of radiation belt electrons observed by SAMPEX

Weichao Tu,[1,2] Richard Selesnick, Xinlin Li,[1,2] and Mark Looper[3]

Received 30 September 2009; revised 17 January 2010; accepted 24 February 2010; published 15 July 2010.

[1] Based on SAMPEX/PET observations, the rates and the spatial and temporal variations of electron loss to the atmosphere in the Earth's radiation belt were quantified using a drift diffusion model that includes the effects of azimuthal drift and pitch angle diffusion. The measured electrons by SAMPEX can be distinguished as trapped, quasi-trapped (in the drift loss cone), and precipitating (in the bounce loss cone). The drift diffusion model simulates the low-altitude electron distribution from SAMPEX. After fitting the model results to the data, the magnitudes and variations of the electron lifetime can be quantitatively determined based on the optimum model parameter values. Three magnetic storms of different magnitudes were selected to estimate the various loss rates of ~0.5–3 MeV electrons during different phases of the storms and at L shells ranging from $L = 3.5$ to $L = 6.5$ (L represents the radial distance in the equatorial plane under a dipole field approximation). The storms represent a small storm, a moderate storm from the current solar minimum, and an intense storm right after the previous solar maximum. Model results for the three individual events showed that fast precipitation losses of relativistic electrons, as short as hours, persistently occurred in the storm main phases and with more efficient loss at higher energies over wide range of L regions and over all the SAMPEX-covered local times. In addition to this newly discovered common feature of the main phase electron loss for all the storm events and at all L locations, some other properties of the electron loss rates, such as the local time and energy dependence that vary with time or locations, were also estimated and discussed. This method combining model with the low-altitude observations provides direct quantification of the electron loss rate, a prerequisite for any comprehensive modeling of the radiation belt electron dynamics.

Citation: Tu, W., R. Selesnick, X. Li, and M. Looper (2010), Quantification of the precipitation loss of radiation belt electrons observed by SAMPEX, *J. Geophys. Res.*, *115*, A07210, doi:10.1029/2009JA014949.

1. Introduction

[2] The outer radiation belt consists of electrons with hundreds of keV to MeV energies and is characterized by large variations in flux. Since the overall structure of the radiation belts and their variability are controlled by the competition between source and loss processes [*Selesnick and Blake,* 2000; *Reeves et al.*, 2003; *Li*, 2004], a detailed understanding of the loss is a required step towards developing comprehensive models for radiation belt electron dynamics, because only when the loss rate is accurately determined will it be possible to appropriately include acceleration and transport processes at the level necessary to compensate for the losses and model the observed enhancements [*Tu et al.*, 2009].

[3] The losses of energetic electrons in the radiation belt may include scattering into the atmosphere, magnetopause shadowing (electrons move out far enough to encounter the magnetopause on open drift trajectories [*Li et al.*, 1997]), and outward radial diffusion [*Shprits et al.*, 2006]. Magnetopause shadowing loss and outward radial diffusion can be implicitly included in the radiation belt radial diffusion model when the phase space density (PSD) at the outer boundary as a function of three adiabatic invariants (μ, K, L) is well defined with a finite L value from the real-time satellite measurements [*Chen et al.*, 2007; *Tu et al.*, 2009]. Electron precipitation losses into the atmosphere are dominant in the heart of the outer radiation belt ($L \sim 4$), which are due to wave-particle interactions that induce pitch angle diffusion.

[4] The quantification of the total electron loss rate should be addressed, not only for the quantification of the acceleration mechanisms in the comprehensive radiation belt dynamics model discussed before but also for particle tracing and radial diffusion codes [e.g., *Elkington et al.*, 2003; *Ukhorskiy et al.*,

[1]LASP and Department of Aerospace Engineering Sciences, University of Colorado at Boulder, Boulder, Colorado, USA.
[2]Laboratory for Space Weather, Chinese Academy of Sciences, Beijing, China.
[3]Space Sciences Department, The Aerospace Corporation, Los Angeles, California, USA.

Copyright 2010 by the American Geophysical Union.
0148-0227/10/2009JA014949

2005; *Shprits and Thorne*, 2004; *Barker et al.*, 2005]. However, uncertainties in the theoretical precipitation loss calculations lead to erratic electron lifetimes used in radiation belt codes. Although theoretical calculations of pitch angle diffusion based on scattering by different types of plasma waves have been carried out since the 1960s [e.g., *Kennel and Petschek*, 1966; *Thorne and Kennel*, 1971; *Summers et al.*, 1998; *Shprits et al.*, 2007], due to the lack of adequate observation of the waves [e.g., *Engebretson et al.*, 2008] and a clear picture of the pitch angle distribution of electrons around the loss cone, electron precipitation processes and the associated loss rates are still not well understood [e.g., *Friedel et al.*, 2002; *Millan and Thorne*, 2007; *Tu et al.*, 2009]. The electron loss rates or lifetimes used in current papers are erratic and can diverge by an order of magnitude. For example, *Shprits et al.* [2005] set the electron lifetime as a constant of 10 days inside plasmapause and empirically as a function of the Kp index (3/Kp) outside the plasmapause, which varied from 0.7 to 4 days in their study events; *Barker et al.* [2005] made the lifetime a function of L and limited it to 3 days at $L = 6$ and 29 days at $L = 4$ in their model; and *Thorne et al.* [2005] concluded that the effective lifetimes of relativistic electron in the outer radiation belt are comparable to a day based on an analysis on microburst observations. This demonstrates that so far we have an unclear understanding of the actual total loss rates.

[5] *Selesnick et al.* [2003, 2004] and *Selesnick* [2006] introduced a drift diffusion model to directly simulate the radiation belt electron data from a low-altitude satellite, SAMPEX, and to estimate the electron loss rate. Low-altitude measurements are most useful in determining the electron precipitation loss rate into the atmosphere, since the electron bounce loss cone opens up at low altitude, and SAMPEX data are ideally suited because of not only its low-altitude orbit but also its large geometric factors and the fast-time resolution of its detector. *Selesnick et al.* [2003] developed the prototype of the drift diffusion model to represent the low-altitude electron distribution, as a balance between azimuthal drift and pitch angle diffusion. The steady decay solution of the model was calculated numerically to fit various data sets during quiet times (when electrons decay steadily) and thus source mechanism was not included in the model. In *Selesnick et al.* [2004], bounce phase dependence was added in the model to simulate the bounce loss cone electrons and detailed physical models for pitch angle diffusion coefficients and electron atmospheric backscattering was used. Then *Selesnick* [2006] reverted to the bounce-averaged model in the work of *Selesnick et al.* [2003] but with a newly added source term and to determine the electron loss rates during geomagnetic active periods. The well-simulated two storm events in the work of *Selesnick* [2006] demonstrated that the drift diffusion model can reasonably represent the low-altitude electron distribution, and the temporal variations of electron loss rate during the two storms indicated that the loss rates typically increase and are highest during the storm main phase.

[6] In this paper, we apply the drift diffusion model method from the work of *Selesnick* [2006] in order to quantify the electron loss rate among various storm events and a much wider L region. In *Selesnick* [2006], the rates and variations of electron loss into the atmosphere are only studied for two intense storms (Dst < −100 nT) and only at $L = 3.5$; here we further explore the temporal variations of electron loss rates for different types of storms, including another intense storm (Dst < −100 nT), a moderate storm (Dst < −50 nT), and a small storm (Dst < −30 nT), from which we will investigate, for instance, on whether the loss is always faster during the storm main phase and whether and how the losses vary with different types of storms. Furthermore, since the outer radiation belt exhibits strong electron flux variations in both time and space, fundamental questions on the spatial variations of electron loss rate into the atmosphere are also important. The spatial variations of the loss rate include both radial dependence and local time dependence. In this paper, we extend the investigation of the temporal variations of electron loss rate over wider L regions, and we can also obtain some knowledge of the local time variations of electron loss rate.

2. Data Description

[7] The main data sets to be used in this work are the energetic electron measurements taken by PET (the Proton/Electron Telescope) instrument [*Cook et al.*, 1993] on board SAMPEX. SAMPEX was launched on 3 July 1992 into a nearly polar orbit with altitude of ~600 km and inclination of 82° [*Baker et al.*, 1993]. It orbits the Earth 15 times each day and has been continuously providing measurements of radiation belt electrons from its launch, covering many different radiation belt conditions. The SAMPEX/PET instrument includes three electron rate counters, measuring electrons with energies from low to high, providing the electron counts every 6 s. They are labeled as P1, counting electrons with $E >$ 0.5 MeV, ELO with $1.5 < E < 6$ MeV, and EHI with $2.5 < E <$ 14 MeV, respectively. P1, unlike the other two counters, is a single detector measurement [*Cook et al.*, 1993]. Note that these energy ranges are only approximate and for reference use. Detailed energy response of each counter is given by the response function [*Selesnick et al.*, 2003], used in our work later. After comparing with PET/PLO proton event data, we have confirmed that there is no significant proton contamination in P1 electron data for the studied events here. Necessary corrections for instrumental deadtime and detector background counts have been performed on the entire PET count rate data used in this work. Additional correction for chance coincidences of the ELO data has also been made (for details please see Appendix A in *Selesnick et al.* [2003]).

2.1. SAMPEX Data Geometry

[8] In order to apply the drift diffusion model to the SAMPEX measurements, some basics about the SAMPEX data geometry need to be understood, for which illustrative cartoons were drawn in Figure 1. On the right side of Figure 1b, the green sphere in the center is the Earth, with the dipole magnet (red square) off the Earth center in real case; the yellow circle represents the SAMPEX low-altitude polar orbit around the earth and the two blue circles (with the left one partly covered by a red curve) illustrate two conjugate magnetic field lines for the same L shell (e.g., $L = 4.5$). Therefore, within one orbit period SAMPEX crosses a given L shell 4 times, labeled as A, B, C and D in white.

[9] For each magnetic field line around the Earth, or each magnetic longitude, there is a bounce loss cone (BLC), the range of equatorial pitch angles (PA) where electrons will precipitate into the atmosphere within one bounce period.

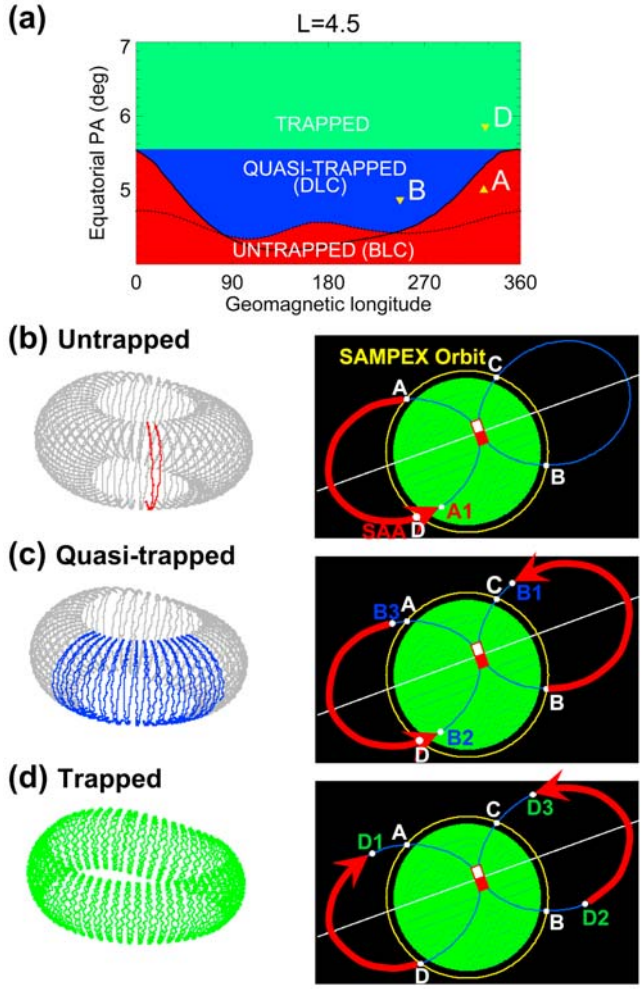

Figure 1. Cartoons illustrating the SAMPEX data geometry. SAMPEX can measure three different electron populations: trapped, quasi-trapped, and untrapped, with their equatorial pitch angle ranges at L = 4.5 shown in Figure 1a. Within each electron population area, a representative point is marked: points A, B, and D respectively. The three points together with another point C are the four detecting positions by SAMPEX at a given L shell within one orbit, shown in Figures 1b, 1c, and 1d, which illustrate how the points A, B, and D detected by SAMPEX can be untrapped, quasi-trapped, and trapped, respectively. The L shell is shown on the left of each panel with the electron trajectories shown in color.

For our model, we define the BLC specifically as the range of equatorial PA with electrons mirror points below 100 km in either hemisphere. The nondipolar nature of the Earth's magnetic field results in nonuniform magnetic field strength at both 100 km and the magnetic equator, hence a longitude-dependent BLC, as shown in the two black curves in Figure 1a. The solid curve is the 100 km BLC angle at L = 4.5 in the Southern Hemisphere, and the dotted curve is for the Northern Hemisphere. So the final 100 km BLC at each longitude is the maximum of these two, with the range of equatorial PA inside the BLC filled by red color in Figure 1a. The peak location of the BLC angle is at ~0° or 360° longitude, where the 100 km magnetic field is the weakest for the fixed L value, and this region is called the South Atlantic Anomaly (SAA). The electrons inside the BLC are classified as "untrapped," since they will be lost within one bounce as illustrated in Figure 1b. Taking point A from Figure 1a inside the BLC as an example, it is detected by SAMPEX in the Northern Hemisphere near the SAA longitudes. But when it bounces to the Southern Hemisphere (the SAA region), the electron mirrors below 100 km (at point A1) and is lost into the atmosphere.

[10] The drift loss cone (DLC) is defined as the range of equatorial PA between the local BLC at one specific longitude and the maximum BLC over all the longitudes, shown in the blue region in Figure 1a. The particles inside the DLC are called "quasi-trapped," such as point B. These particles can stay trapped at some longitudes (B to B1 in Figure 1c), but when they drift to the SAA region, they will get lost (at B2). Therefore, the particles inside the DLC cannot stay longer than a drift period. However, for particles outside the DLC, the green area in Figure 1a, they will stay trapped at all longitudes (assuming no pitch angle scattering). We take point D in Figure 1a as an example and show the geometry in Figure 1d: detected by SAMPEX near the SAA region at point D, then bounce to D1, and then D2 to D3 after drift.

2.2. PA-Longitude Plot

[11] As we described, points A, B, C and D are the four measuring locations of SAMPEX at a given L shell within one orbit. And from Figures 1a–1d, we understand that SAMPEX can observe all the three different electron populations: trapped, quasi-trapped, and untrapped. In Figure 2a, we plot out the maximum equatorial PA of electrons measured by SAMPEX at a given L shell within 1 day versus geomagnetic longitude. It used the pattern in Figure 1a as the background. The maximum equatorial PA corresponds to detected electrons with local PA equal to 90° or mirroring at SAMPEX locations. The yellow triangles represent the data points detected by SAMPEX at L = 4.5 within the day 13 February 2009. Note that the geomagnetic longitude is calculated under the Corrected GeoMagnetic coordinates (CGM) using the IGRF model [*Gustafsson et al.*, 1992] and the L shell value used is the McIlwain L [*McIlwain*, 1961] obtained by using the IGRF model. Since the Earth is rotating underneath SAMPEX's orbit, the data can reach full-longitude coverage after 1 day (at least half a day). And since SAMPEX orbits the Earth 15 times per day, within 1 day it crosses a given L shell ~60 times, resulting in ~60 data points in the figure. Upward triangles indicate crossings in the Northern Hemisphere and downward triangles are in the Southern Hemisphere. Based on the maximum observed PA, the detected electrons can be approximately classified as trapped (in the green area), quasi-trapped (in the blue area), and untrapped (in the red area).

[12] There will be certain errors from the approximate electron classification based on the maximum observed PA, since not all the measured electrons will have local PA equal to 90°. However, it is virtually unachievable for SAMPEX to provide the exact local PA of measuring electrons, given the wide look angle of its detector. So the possible scenarios are some so-called "trapped" electrons in Figure 2a can be actually quasi-trapped (due to local PA < 90°) or some "quasi-trapped" electrons are actually untrapped. But the classified as "untrapped" electrons will be truly untrapped,

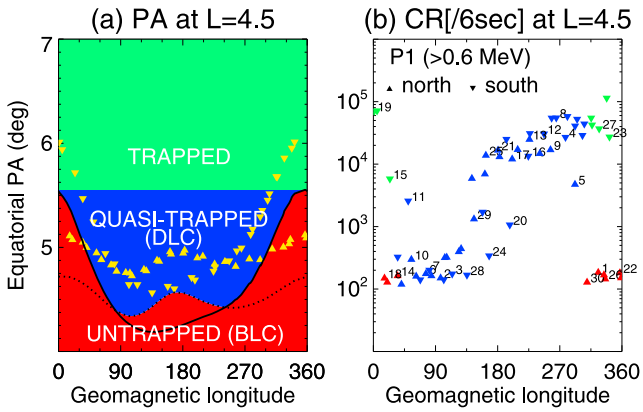

Figure 2. Figure 2a shows the maximum equatorial pitch angle distribution of electrons measured by SAMPEX at L = 4.5 within the day 13 February 2009 versus geomagnetic longitude. The maximum observed pitch angle data are in yellow, which fall into three categories in the colors same with Figure 1a. The upward triangles were detected in the Northern Hemisphere and the downward ones were in the Southern Hemisphere. Figure 2b illustrates the count rate distribution of the same data points in Figure 2a, where the first 30 crossings at L = 4.5 within that day are numbered in chronological order, with the trapped electrons in green, the quasi-trapped ones in blue, and the untrapped ones are in red.

and there are no trapped electrons falling into the "DLC" region. In this work, we only use this approximate classification as an intuitive reference when we want to qualitatively discuss the physical behavior of electrons in the three populations. In the quantitative model, the approximation is not really used, which will be clearer later.

2.3. Count Rate-Longitude Plot

[13] Now we know the approximate data PA distribution in longitude as shown in Figure 2a. The corresponding count rate (CR) distribution for the same data points is shown in Figure 2b. It illustrates the logarithm of the electron counts per 6 s detected by P1 within the same day at L = 4.5, plotted over geomagnetic longitude. Each CR data point in Figure 2b corresponds to one PA data point in Figure 2a at the same geomagnetic longitude. So there are also 60 data points. Again, upward triangles are for Northern Hemisphere crossings and downward triangles are in the south. Note that here the ~60 points within 1 day are aligned according to their longitudes, not in time sequence. For the reference of time, the first 30 crossings on 13 February 2009 are numbered in chronological order in Figure 2b. Two consecutive crossings at L = 4.5 are either ~15 min or ~30 min apart in time, depending on their located hemispheres.

[14] After categorization from the PA distribution in Figure 2a, the trapped electrons are plotted in green for consistency; similarly, untrapped data points are in red and data inside the DLC are in blue. From the CR distribution plot, we notice that high CR detected in the Southern Hemisphere (green downward triangles) near the SAA longitudes are stably trapped electrons. Low fluxes in the same longitude range but in the Northern Hemisphere (red upward triangles) are electrons in the BLC. They generally have the lowest data rates. And the low CR to the east of SAA in the DLC, from both north and south, gradually increase with longitude as the DLC filled in by pitch angle diffusion along with the eastward electron drift. The generally reasonable count rate distributions of the three different electron populations over longitude demonstrate that the approximate classification of the detecting electrons is qualitatively acceptable. Since the DLC electrons cannot survive a drift period, the relative trapped and quasi-trapped intensities can indicate the electron loss rate. Still, we simulate these data with the drift diffusion model in order to quantify the electron loss rate.

3. Model Description

[15] Since the observed electron flux variation is a complicated balance between loss and energization, for any quantitative study, a physical model is needed. Here we follow the drift diffusion model of *Selesnick* [2006] to simulate the low-altitude electron distribution from SAMPEX. The model is governed by the equation:

$$\frac{\partial f}{\partial t} + \omega_{\mathrm{d}} \frac{\partial f}{\partial \phi} = \frac{\omega_{\mathrm{b}}}{x} \frac{\partial}{\partial x}\left(\frac{x}{\omega_{\mathrm{b}}} D_{xx} \frac{\partial f}{\partial x}\right) + S \qquad (1)$$

where $f(x,\phi,t)$ is the bounce-averaged electron distribution function at a given L shell and kinetic energy E, as a function of $x = \cos\alpha_0$, where α_0 is the equatorial pitch angle, drift phase ϕ, and time t; ω_{d} is the bounce-averaged drift frequency (assumed α_0 independent for numerical simplicity since the variations from α_0 are within a factor of 1.5); ω_{b} is the bounce frequency; D_{xx} is the bounce-averaged pitch angle diffusion coefficient; and S is the source rate. In the model, there are 90 grid points in ϕ and 135 grid points in $x = \cos\alpha_0$, covering from α_0 = 90° to DLC until BLC. The left hand side of equation (1) is an advective time derivative including the effects of azimuthal drift, and the first part of the right hand side represents pitch angle diffusion. The diffusion coefficient is

$$D_{xx} = D_{dawn/dusk} \tilde{E}^{-\alpha} \frac{1}{10^{-4} + x^{30}} \qquad (2)$$

where $\tilde{E} = E/(1\ \mathrm{MeV})$. The constant 10^{-4} is included for numerical stability at low x values (or high equatorial pitch angles). In this case, the x dependence in D_{xx} will be distorted to some extent from the exponential x^{-30} for low x values but remain x^{-30} for high x values. The power index 30 on x is chosen as a typical value by fitting both the high altitude data from the polar satellite and the low altitude data from SAMPEX in the work of *Selesnick et al.* [2003]. Hence, the pitch angle diffusion is faster for electrons with larger equatorial pitch angles, consistent with the essentially flat pitch angle distributions at equatorial pitch angles around 90°. Even though the model results in [*Selesnick et al.*, 2003] showed some variations of the power index on x, ranging from 20 to 60, since the model solution performs insensitive to this index when it exceeds 20, especially in the low α_0 region, fixing it as 30 is reasonable here. D_{dawn} and D_{dusk} are independent parameters, which are separated for the purpose of investigating the possible magnetic local time (MLT) dependence of the diffusion rate, taking advantage of the geometry that SAMPEX orbital plane was basi-

cally in the dawn-dusk sector during the three events described in the next section. D_{dusk} is for 0–12 h MLT with D_{dusk} for the other half. The source rate function is

$$S = S_0 \tilde{E}^{-\nu} \overline{g}_1(x)/p^2 \tag{3}$$

where $\overline{g}_1$ is the lowest-order eigenfunction of the drift-averaged pitch angle diffusion operator, p is the electron momentum for a given E and S_0 is always positive. Here the source mechanism is unspecified which could be either radial diffusion or local heating. Overall, the free parameters in the model are D_{dawn}, D_{dusk}, α, ν, and S_0. As represented by the model equation, the observed low-altitude energetic electron distribution is a balance of azimuthal drift, pitch angle diffusion into the upper atmosphere, and possible concurrent sources.

[16] Given the free parameter values, appropriate initial conditions and boundary conditions for $f(x,\phi,t)$, equation (1) can be solved numerically combining operator splitting, Crank-Nicolson and upwind differencing methods. The sample solutions for the electron distribution f as a function of longitude and equatorial pitch angle at two different L shells with different sets of parameter values are shown in Figure 1 in *Selesnick et al.* [2003]. The three model solutions on the left-hand side panels (a)–(c) in Figure 1 of *Selesnick et al.* [2003] show that for high values of the ratio $D_{xx}/\omega_{\mathrm{d}}$, diffusion is dominant over drift and losses occur over all longitudes; as the ratio $D_{xx}/\omega_{\mathrm{d}}$ decreases, the drift becomes more significant over diffusion and losses start to occur over a smaller longitude range to the west of SAA. And the other three solutions on the right-hand side panels (d)–(f) in Figure 1 of *Selesnick et al.* [2003] demonstrate how different values of D_{day} and D_{night} work in the model (in our case, it would be $D_{dawn/dusk}$, which works in a similar way).

3.1. Boundary Conditions

[17] The boundary conditions used in the model include: first, $f = 0$ at the edge of the BLC. So the BLC distribution versus geomagnetic longitude forms the longitude-dependent lower boundary of the simulations. In other words, the model requires the BLC to be relatively empty, which will be true under the slow diffusion (or weak diffusion) assumption. If the strong diffusion limit is approached, when the electrons scatter into the loss cone even faster than the atmosphere can remove, the assumed boundary condition will break down [*Schulz and Lanzerotti*, 1974]. More discussions about this assumption will be included in section 5 combined with the event study results. The second boundary condition at the high equatorial PA end is $\partial f/\partial x = 0$ at $x = 0$ (or $\alpha_0 = 90°$) for each ϕ or the PA distribution at 90° is flat. The initial model energy spectrum for a specific storm event is obtained by best fitting the stably trapped electron flux from the PET/pulse height analysis (PHA) data from ELO and EHI along with the count rate data from P1 for the first time interval before the storm (please refer to *Mewaldt et al.* [2005] for a description of similar PHA spectrum calculation but for solar electrons). The PET/PHA events data are a subset of the ELO and EHI data being pulse height analyzed, which provides a measure of the energy deposit in each detector from individual electrons [*Cook et al.*, 1993, *Mabry et al.*, 1993]. Besides, the initial model pitch angle distribution is considered the same shape with $\overline{g}_1(x)$ in equation (3) but normalized by the initial energy spectrum and assumed uniform over all the longitudes.

3.2. Energy Spectrum

[18] The model was run at eight logarithmically spaced energies from 0.5 to 5.66 MeV. The model results at other energies are obtained by exponential interpolation or extrapolation. Now we have the modeled phase space density, f, as a function of x, ϕ, and E at each time step. Model flux, j, is calculated based on the equation $j = p^2 f$. However, in order to generate the model count rates to directly compare with the observations from P1, ELO, and EHI, the counter response function R, as a function of energy and polar angle from the telescope axis of a incoming particle, is needed to integrate the modeled flux over both local pitch angles and energies for a measured electron count rate from a given counter, at specific time and location and with corresponding satellite orientation. The details about the PET response functions and the count rate simulation are introduced in the Appendix of *Selesnick et al.* [2003].

3.3. Parameter Tuning

[19] Now we understand how the drift diffusion model works to simulate the count rates from different counters at different locations and times but not how to constrain the five free parameters in the model. As we discussed in section 2, the count rate data showed considerable variations over geomagnetic longitudes, indicating a delicate balance of azimuthal drift and pitch angle diffusion. Therefore, to fully constrain the model free parameters, primarily in the pitch angle diffusion rate and source rate, the model requires data with full-longitude coverage, such as the count rate data shown in Figure 2b. Since SAMPEX can only cover all longitudes for at least half a day, the model is not capable of resolving the parameter variations on time scales less than 12 h. Thus, when simulating one storm event, the data and the model are processed basically on a daily basis; except for during the main phase, when the data may exhibit rapid change, the data and simulation interval is switched to half a day. Then within one data interval (1 day or half a day), the parameters are iteratively tuned to achieve the least mean square difference between the logarithms of the modeled electron rates (p_i) and the data (d_i), defined as

$$\mathrm{K}^2 = \frac{\sum_{i=1}^{n} (\lg d_i - \lg p_i)^2}{n}, \tag{4}$$

where n is the total number of data points within the interval. The quasi-Newton method was used in the parameter iteration [*Tarantola*, 2005]. The model results $f(x,\phi,E)$ from the end of last interval are passed as the initial condition into the current interval within which another parameter tuning initiates.

3.4. Electron Lifetime

[20] Electron lifetime τ is the e-folding time scale defined for a steady decay state, which represents the loss rate only if the parameters are unchanged for a period much longer

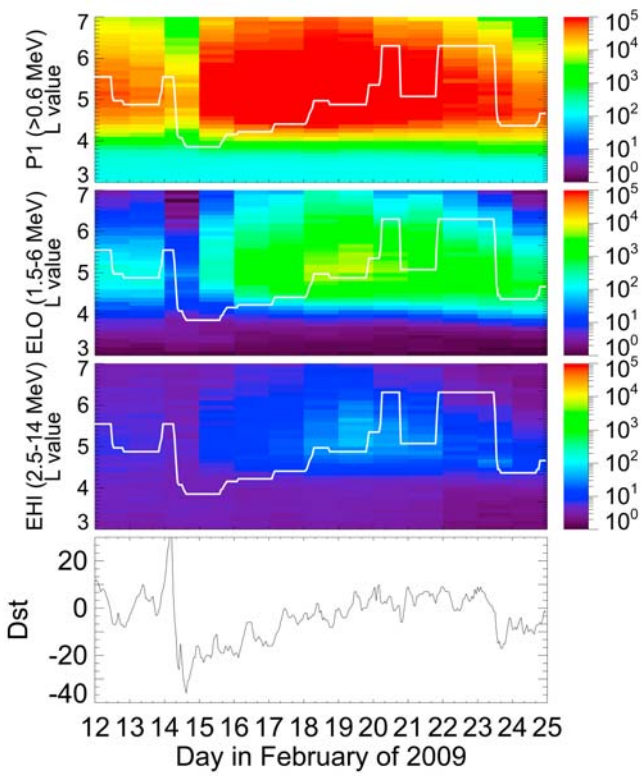

Figure 3. The top three panels show the electron count rate variations over the February 2009 storm from 12 to 25 February 2009 detected by three SAMPEX/PET counters: P1, ELO, and EHI, respectively. The count rates, in units/6 s, are daily-averaged in time axis (X axis), color-coded in logarithm (color bar on the right), and sorted in L (L bin: 0.1 in Y axis). The superposed white curves illustrate the plasmapause locations. The bottom panel is the Dst data during this storm.

than $1/(\lambda_2\overline{D})$ (see explanations of $\overline{D}$ and λ_2 below). After obtaining the optimum set of parameters for each time interval in our model solutions, the actual pitch angle diffusion rates at different energies can be determined using equation (2). Then the electron lifetime for a specific energy can be approximately inferred as

$$\tau = 1/\left(\lambda_1\overline{D}\right) \tag{5}$$

where $\overline{D}$ is the longitude-averaged model diffusion coefficient defined as $\overline{D} = (D_{dawn} + D_{dusk})\tilde{E}^{-\mu}/2$ and $\lambda_1 \approx 100$ is the lowest-order eigenvalue of the normalized diffusion operator (the first terms on the RHS of equation (1) involving $\partial/\partial x$, divided by $-\overline{D}$). λ_2 above is the second-order eigenvalue. Equation (5) is analytically derived from solving the drift-averaged pitch angle diffusion equation (equation (1) without the drift and source terms and with $D_{xx} = \overline{D}\frac{1}{10^{-4}+x^{30}}$), and λ_1 is calculated numerically for L values from 3.5 to 6.5. Based on this, the electron lifetimes at different energies for each time interval can be easily estimated from the determined diffusion coefficients.

[21] One thing we would like to clarify is that our model approach in estimating the electron pitch angle diffusion rate is different from the wave study approach using quasi-linear theories [e.g., *Summers et al.*, 2007; *Li et al.*, 2007]. They are complementary approaches, both of which have to assume parameters. For example, *Li et al.* [2007] made certain assumptions on the spectral distribution of the wave power, the ratio of plasma frequency to electron gyrofrequency (f_{pe}/f_{ce}), the distribution of wave normal angles, local time content, etc. But our model assumes the form of D_{xx} in equation (2) with free parameters and estimates the pitch angle diffusion rate based on parameter fitting to real-time data, without explicitly using the wave and plasma properties. An advantage is that we can estimate the electron precipitation loss rate of many simultaneous processes as shown in section 4.

4. Event Study

[22] In this paper, we selected three different types of storms for detailed study: one of which is a small storm in February 2009, the other is a moderate storm in March 2008, and the third is an intense storm in September 2002. The first two are during the current deep solar minimum, and the last one is right after the last sunspot maximum. For each event we ran the drift diffusion model for four different L regions (L = 3.5, 4.5, 5.5, and 6.5), hence for four different data sets, one at each L. Then each data set was divided into several daily or half a day intervals to achieve full-longitude coverage within each interval. Here we first discuss the simulation results for the February 2009 storm in detail.

4.1. February 2009 Event: A Small Storm

[23] The overall electron count rate variations over the February 2009 storm were shown in Figure 3 as a function of L shell (Y axis) and time (X axis). The logarithm of daily-averaged count rates are color coded according to the color bar shown on the right side of the plot, one panel for each rate counter with the energy range shown on the left. Electron rates are binned in bins of 0.1 L in Y axis direction. The white curve on top of the color spectrum plot shows the plasmapause location calculated using an empirical model in the work of *O'Brien and Moldwin* [2003]. Although the storm was small with Dst only reaching ~−40nT (see the Dst profile in the fourth panel of Figure 3), it caused very dynamic radiation belt responses: the electron count rates dropped down significantly during the storm main phase, recovered during the early recovery phase and increased above the prestorm levels later in the recovery phase.

4.1.1. Count Rate Simulations

[24] The drift diffusion model was used to simulate this event, with the count rate data and the simulation results at L = 4.5 shown in Figure 4. The count rates from three different rate counters are plotted as a function of geomagnetic longitude within each interval, with corresponding time period specified on the top of each panel. According to the bottom Dst profile in Figure 3, Figure 4a is during a quiet day prior to the storm; Figure 4b immediately follows Figure 4a in time and includes the storm main phase (lasting about half a day); Figure 4c is during the early recovery phase and Figures 4d–4f constitute the late recovery phases in time order; the six of which, in total, shows the evolution of the low-altitude electron count rates during the storm event. Filled data points are the measured electron count rates, and the open data points show the simulations that are the best fits to the data. Since the EHI count rates were very low during this event, close to

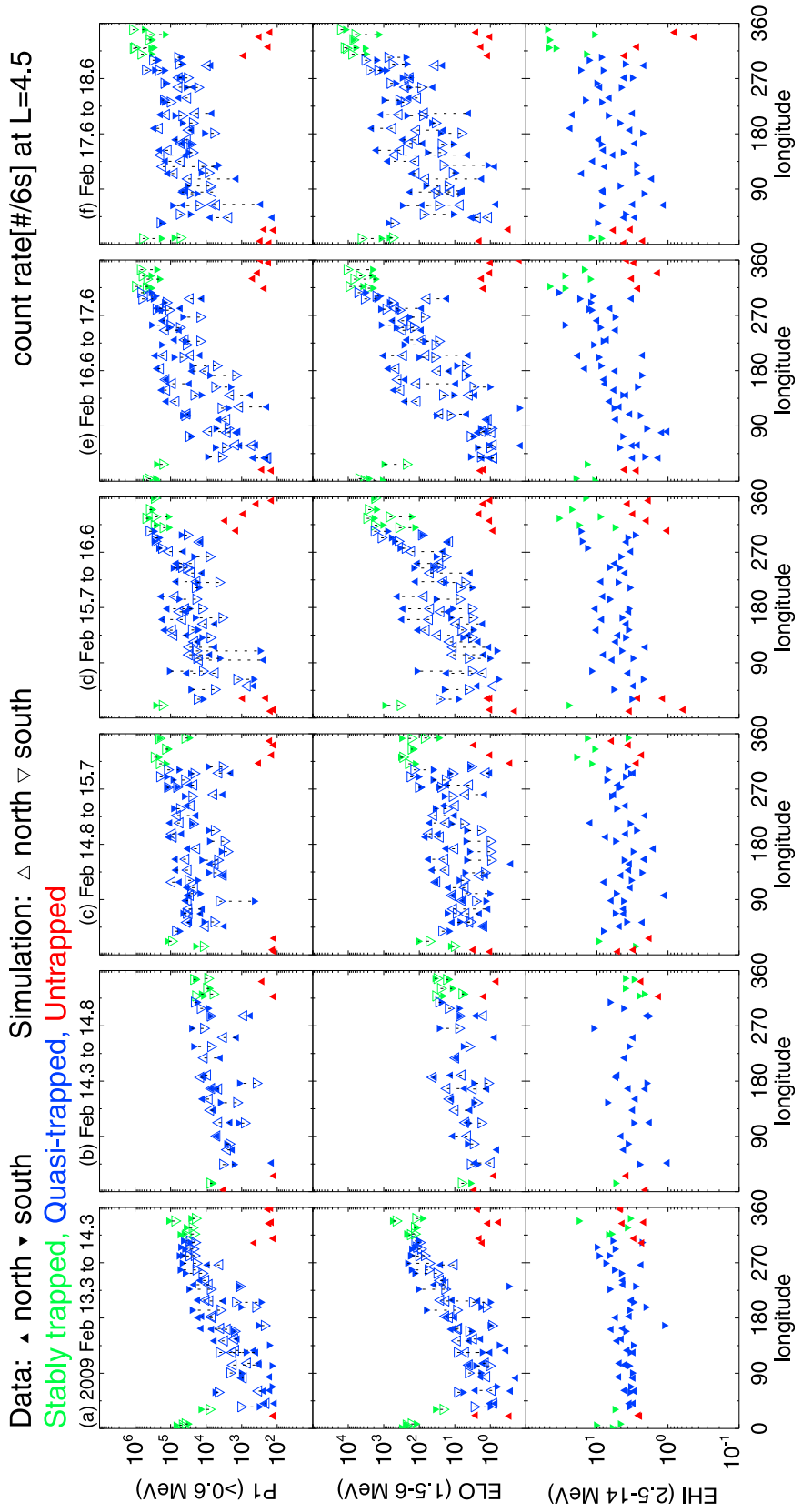

Figure 4. Electron count rate data (filled triangles) and model simulations (open triangles) versus geomagnetic longitude for the three rate counters at $L = 4.5$ during (a) a quiet prestorm interval, (b) storm main phase, (c) early recovery phase, and (d, e, f) late recovery phases of the February 2009 storm. The count rate pattern (color and shape) is the same with that in Figure 2b.

the background counts, uncertainties due to Poisson counting statistics, which are significant for the low fluxes, could be significant in the EHI rate data. Therefore for this event, we did not include the EHI count rates in the model simulation.

[25] During the quiet time before the storm (Figure 4a), the count rates versus longitude pattern can be understood with reference to Figure 2b. Three electron populations were identified: stably trapped electrons near the SAA longitudes (green downward triangles); untrapped electrons in the same longitude range but with lowest count rates (red upward triangles); and the DLC electrons in the middle (in blue). And the low count rates in the DLC increased eastward with longitude because of the azimuthal drift, which indicates that the DLC was only filled in gradually by pitch angle diffusion with the drift, hence suggesting a relatively low pitch angle diffusion rate during this interval. We did not need to turn on the source to fit this data set reasonably well. Note that since our model assumes that the BLC is empty, which is a good assumption here considering the BLC data (red points) are near background, the data points within the BLC cannot be simulated.

[26] In Figure 4b, the storm main phase, we noticed that the stably trapped population near 0° and 360° longitude (green triangles) decreased significantly, which was a result of the fast electron losses into the Earth's atmosphere, suggesting enhanced pitch angle diffusion. The decrease was more significant for higher energy channels (ELO), indicating faster pitch angle diffusion for higher energy electrons. So the energy dependence index α should be negative in equation (2). The quasi-trapped population in the DLC from ~45° to 315° longitudes (blue triangles) also decreased during the storm main phase but less significantly compared with the stably trapped population. Furthermore, the DLC electrons were almost on the same count rate level with those stably trapped ones and were relatively flatly distributed over the longitude. These indicated that the DLC was fully filled by pitch angle diffusion from the trapped electrons and the diffusion coefficient was required to increase significantly to produce such fast diffusion. No source was required to fit these data reasonably well.

[27] During the early recovery phase (Figure 4c), the trapped electron count rates (green triangles) almost recovered to the pre-storm levels. This increase continued during the late recovery phase (Figures 4d–4f), leading to the trapped count rates much higher than the prestorm values, which required a continuous active source during the exhibited recovery phase (Figures 4c–4f). On the other hand, the pitch angle diffusion rate returned to a lower value during the recovery phase, based on the decreased DLC electron count rates and the reappearance of the evident eastward increase of the DLC content over longitude.

4.1.2. Model Fit Results

[28] The descriptions above for each interval of the February 2009 storm tell us how the model parameters were adjusted to fit the data during each interval and the simulation data comparisons in Figure 4 illustrate the quality of the fits. Based on the best fit simulations, we can obtain the optimum parameter set for each interval and then infer the source and loss rates at $L = 4.5$ for the storm event, as shown in the second column of Figure 5, together with results for other L in rest of the columns. The first row illustrates the variations of the model trapped electron intensity, j_0 (at 90° equatorial pitch angle), versus time at six different energies: 0.5, 0.71, 1.0, 1.41, 2.0, 2.83 MeV, shown in different colors. The black curve in the background is the Dst index for this storm. The second row shows the equatorial source rate $S_0\tilde{E}^{-\nu}$ for each energy channel. And the bottom row compares the derived electron lifetime in days and the electron replenish time (model equatorial intensity/source rate) in days, from which we can tell which one of the two processes, loss and source, is faster. The lifetime was calculated from the parameterized pitch angle diffusion rate using equation (5). Here we discuss the fitting results for all four L regions together. But since there were very little dynamics at $L = 3.5$ and the count rates there were very low, as illustrated in the color spectrum plot of February 2009 storm (Figure 3), the fitting results at the first column for $L = 3.5$ could involve bigger errors and are not included here in the discussion.

[29] For $L = 4.5$ to $L = 6.5$, we notice that the trapped electron flux, j_0, decreased during the storm main phase, more significantly for higher energies, and started increasing at the early recovery phase, when the source was needed in the model. For all the three L, the increase of j_0 in the early recovery phase was more rapid for the lower energies (0.5 and 0.71 MeV), with j_0 reaching and then growing above the prestorm values within 1 day after the start of the recovery phase. However, j_0 at higher energies exhibited a two-boost increase during the recovery phase, a gradual raise at the early recovery phase and a more rapid one at the second time interval of the recovery phase, resulting in j_0 also higher than the prestorm values but in the late recovery phase. And the trapped fluxes for all L and energies went relatively steady during the late recovery phase even though the source rates were variable, as shown in the second row of Figure 5.

[30] Since we are most interested in the loss rates, we need to look at the solid lines in the third row in more detail. For the typical quiet time before the storm, the electron lifetime is above 10 days for all energies at $L = 4.5$–6.5, with energy dependence index, α in $D_{xx} \propto E^{-\alpha}$, being negative, and the absolute value of α bigger at larger L. The loss rate became significantly faster during the storm main phase, with α still being negative. For the lower energies the fastest loss occurred at $L = 6.5$, but for energies >2 MeV, the fastest loss was at $L = 5.5$, on the scale of hours. This indicates that the radiation belt can almost deplete within this main phase interval (~half a day), estimated by the equation $f = f_0 e^{-t/\tau} = f_0 e^{-12\ \mathrm{h}/1\ \mathrm{h}} \approx 0$, consistent with the depletion of j_0 for 2.83 MeV at $L = 5.5$. At the early recovery phase, the loss rates quickly returned to low values, but with the sign of the energy dependence index flipped compared with the prestorm index. For $L = 4.5$, the loss rates were still faster than the quiet time, but for $L = 5.5$ and 6.5, they almost returned to the prestorm levels. In the late recovery phase, the energy dependence changed back for $L = 4.5$ and 5.5 (α returned to negative), but for $L = 6.5$, α remained positive all the time over the recovery phase.

[31] Here we would like to clarify two concepts before moving on to the next event: the electron lifetime and the electron precipitation rate. The former is directly related to the pitch angle diffusion rate, D_{xx}, as shown in equation (5); while the latter depends on both D_{xx} and the available trapped intensity. For example, by comparing the trapped and DLC fluxes (green and blue triangles) in Figures 4b and 4d, we see

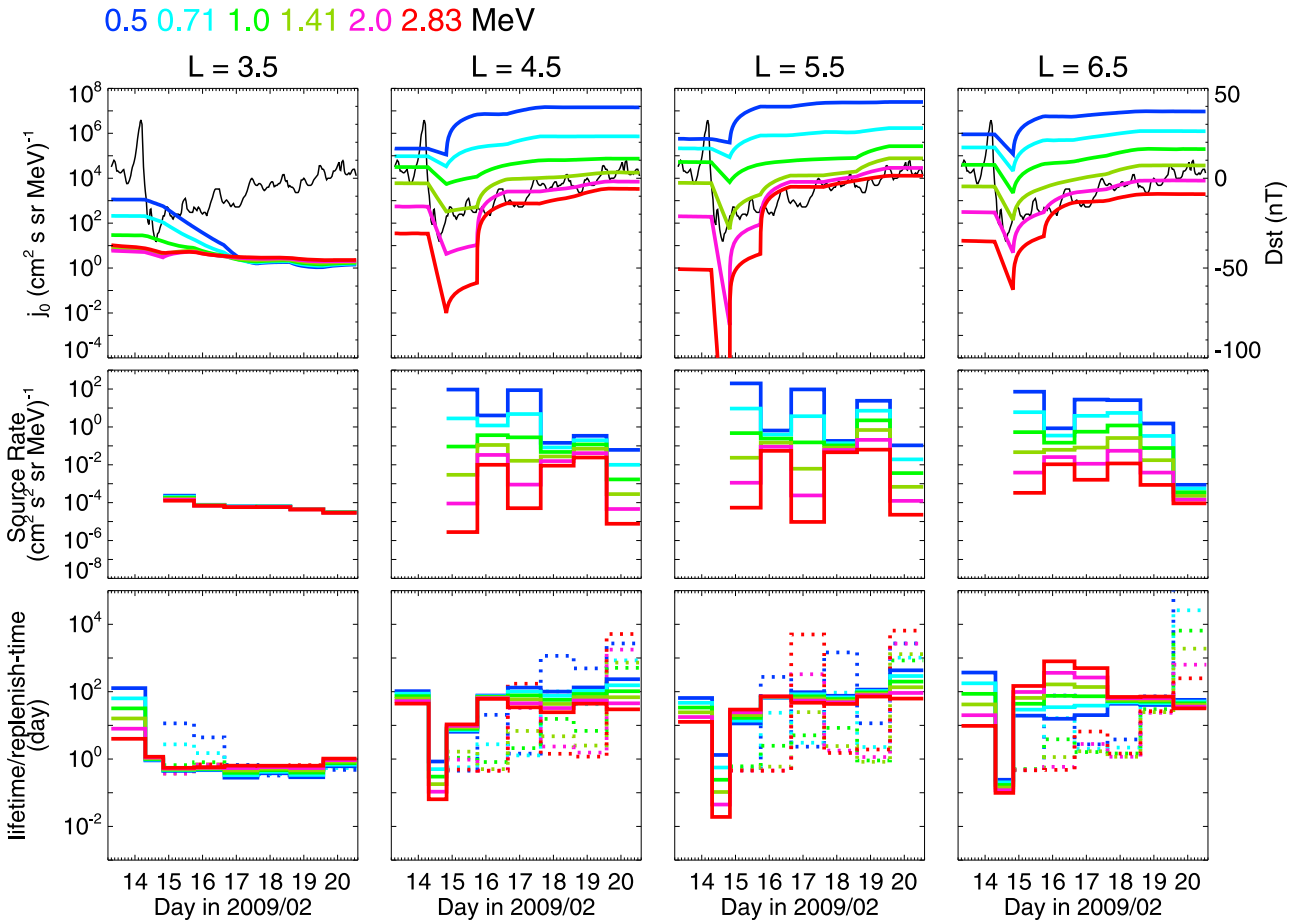

Figure 5. Model results from the optimum model fits to the data for the February 2009 storm at various L locations over a range of electron energies represented in different colors (color bar on top). One column is for one L. The first row shows the equatorial intensities; the second is the equatorial source rates, and the bottom row compares the derived electron lifetimes (solid lines) and the electron replenish times (dotted lines).

that even though D_{xx} was much higher (or electron lifetime is much shorter) during the storm main phase of February 2009 storm, the precipitation level during the recovery phase in Figure 4d could be comparable to or even higher than that in the main phase.

4.2. March 2008 Event: A Moderate Storm

[32] For the second storm, which occurred in March 2008, the variations are basically the same, since both storms were not big storms during solar minimum. Figure 6 provides an overview of the electron count rate variations during this storm event, in the same format as Figure 3. Here we did not show the data simulation plot for this storm, which is similar to Figure 4 for February 2009 storm. Only the model fitting results were illustrated in Figure 7, in the same format as Figure 5. In the trapped intensity plot, we also see the two-boost increase of j_0 for higher energies. But compared with the results of February 2009 storm, for high energies the trapped flux did not return to the prestorm level after the recovery phase. One thing to notice is that the energy spectrum of j_0 after the storm became much softer than the prestorm spectrum, mainly from the softer energy spectrum in the source rate. Similar to the February 2009 storm, source was only required to be on during the storm recovery phase for this event at all L regions. For the loss rates, the energy dependence index α was also negative during the storm main phase over all L regions but it is generally negative for the other storm phases as well, even for $L = 6.5$, which was different from the February 2009 storm. Lifetime can also be as short as hours during the main phase at higher energies (>1 MeV) over broad L regions. After the early recovery phase, the loss rate at $L = 4.5$ returned to the quiet time level but for $L = 5.5$ and 6.5, the loss rates remained elevated.

4.3. September 2002 Event: An Intense Storm

[33] The September 2002 storm was quite different, considering it was a much more intense storm right after the solar maximum. From Figure 8 we found that now $L = 6.5$ was the place that had little dynamics and lower count rates, since the peak rate location was around $L = 4$. Notice that the L ranges in Figure 8 were extended to $L = 2$–7, from $L = 3$–7 in Figures 3 and 6 for the other two storms. The entire outer radiation belt was compressed during solar max and the plasmasphere was also displaced inward, as illustrated by the white plasmapause location curves. For this event, EHI counts were included in the model simulation since

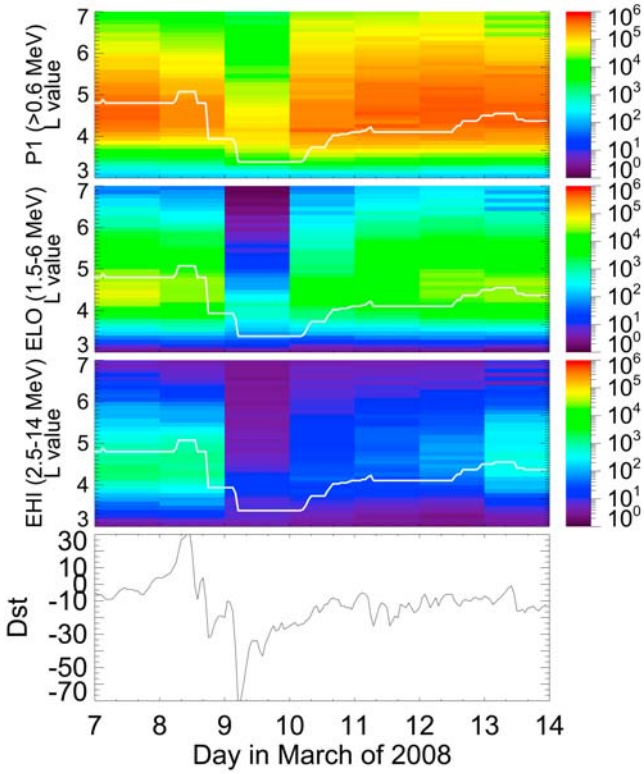

Figure 6. Electron count rate variations and Dst profile over the March 2008 storm. The configuration is the same with Figure 3.

they were much higher. The model fitting results are shown in Figure 9. At small L, the decrease of j_0 during the storm main phase was still more significant at higher energies, most obvious at $L = 4.5$, and for some of the high energies, j_0 did not recover to the prestorm level after the storm. Source was needed from the early recovery phase. However, for higher L regions ($L = 5.5$–6.5), there was little energy dependence in the loss rates over the whole storm and source was not required until the second recovery interval. And the trapped fluxes generally did not recover after the storm at high L, even for low energy fluxes. The softening of the flux energy spectrum was most evident at $L = 3.5$. For this storm, the lifetime of the prestorm interval was less than 10 days but longer than 1 day for almost all energy electrons, and with positive energy dependence index, both of which were different from the other two storms in solar minimum. However, much the same as the first two storms, the loss was the fastest during the storm main phase and with a negative α (faster loss at higher energies) over wide L regions. In the late recovery phase, the loss rate returned to typical prestorm levels but with the sign of α remained negative at $L = 3.5$ and 4.5 (the peak flux locations). Another distinct feature about this storm is during the main phase at $L = 4.5$, the lifetime at higher energies can be less than 10^{-3} day (~minute). This loss was so fast that the weak diffusion assumption broke down. Then the current drift diffusion model was not accurate in determining the lifetime. This will be discussed in the next section. But for this event the DLC electron count rate data from ELO did show an abrupt drop by >2 orders of magnitude within tens of minutes from the end of the first interval to the start of the main phase interval, indicating the electron lifetimes for the high-energy electrons were on the order of minutes and proving our model still provided a realistic estimate of the loss rate.

5. Discussion

5.1. Common Feature: Fast Losses for All Energy Electrons With Faster Losses at Higher Energies During Storm Main Phases

[34] In the event study we have simulated three different types of storms, with minimum Dst around −40, −70, and −180 nT, respectively. All the simulation results from the best fits of the three storms at four different L locations suggested some common features: that the loss of energetic electrons was always the fastest during the storm main phase and with more efficient loss at higher energies; the corresponding lifetimes for the high energies can be as short as hours for the small and moderate storms and minutes for the intense storm; and the fast losses (with time scales shorter or on the order of an hour) occurred over wide L regions around the peak electron flux location, $L = 4.5$–6.5 for the February 2009 and March 2008 storms and $L = 3.5$–5.5 for the September 2002 storm. As introduced, the drift diffusion model can also resolve certain local time variations of the electron loss rate based on the local time coverage of SAMPEX's orbit. Based on the fitting results of D_{dawn} and D_{dusk} for three storms, very little local time dependence was observed for the fast losses during the storm main phases, except for at $L = 5.5$ in February 2009 storm, which will be discussed in detail later.

[35] Therefore, fast precipitation losses of energetic radiation belt electrons were confirmed during the storm main phases, with higher energy electrons lost faster, over wide range of L regions, over the SAMPEX-covered local times, no matter what the magnitude of the geomagnetic storm was. What are the possible loss mechanisms for these fast losses? Electromagnetic ion cyclotron (EMIC) waves were suggested as capable of providing rapid loss of relativistic electrons on time scale of hours during storms [*Meredith et al.*, 2003; *Albert*, 2003], with similar energy dependence in the pitch angle diffusion rates under the assumed EMIC waves and plasma properties [*Summers et al.*, 2007]. But they were believed to be preferentially excited along the duskside of the plasmasphere and in the regions of plumes [e.g., *Erlandson and Ukhorskiy*, 2001; *Summers and Thorne*, 2003], which is not sufficient to explain the fast losses over wide L regions and local times in some of our results. However, the fast electron precipitation during the storm main phase indicates that some intense wave activity much be present to account for the fast pitch angle diffusion of electrons. Therefore, the underlying electron loss mechanism so far can only be understood as some quick scattering processes, which function preferably on higher energy electrons. The specific wave mode that caused the loss deserves further study and observational proof, which could also be a comprehensive effect from the gyroresonant wave-particle interactions with various magnetospheric wave modes.

[36] **Strong diffusion:** The electron lifetimes at $L = 4.5$ during the main phase of the most intense storm, the Sep-

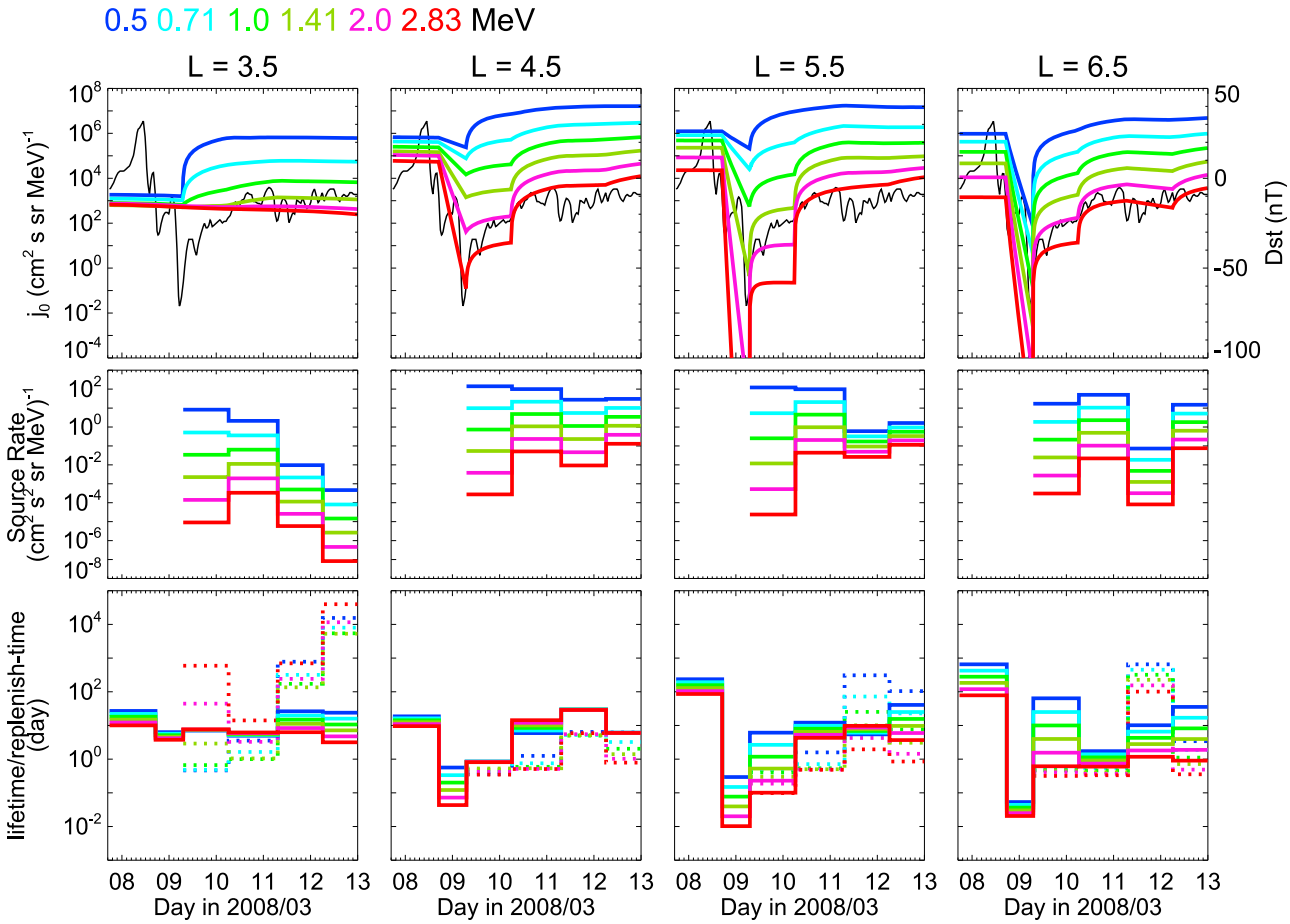

Figure 7. Model results for the March 2008 storm at different L with the same configuration in Figure 5.

tember 2002 storm, were on the order of minutes for high energy electrons. Should they be classified as strong diffusions? Under strong diffusion, the pitch angle distribution of electrons is isotropic and the assumption that BLC is relatively empty in the drift diffusion model will be violated. So we checked the strong diffusion limits for the same energy ranges of the results in Figure 9. The calculated electron lifetimes with respect to the strong diffusion rates for 0.5–2.83 MeV electrons at L = 4.5 are all on the order of 10^{-3} day [*Schulz and Lanzerotti*, 1974, pp. 77–80]. Therefore, according to the results shown in Figure 9, the losses of 2.0 and 2.83 MeV electrons at L = 4.5 in the September 2002 storm main phase are within the strong diffusion range, and they break the weak diffusion assumption in the model. These are also consistent with the count rate versus longitude plot at L = 4.5 during this time period (not shown in this paper), where the trapped and DLC rates seemed to decrease down to the level of the BLC rates. Under this situation, the current drift diffusion model cannot accurately determine the electron loss rates but only provide an approximation. But since the strong diffusion only happens in extreme cases, perhaps only for very intense storms, for electrons at certain range of energies, and at limited time and locations, our model is still valid for the other cases and is generally applicable. It would be another project to improve the model for the strong diffusion case.

5.2. Other Features of Electron Lifetimes

[37] After discussing the loss rates during the storm main phases, we look into others features of the losses over all the storm phases in the three events. The first is about the energy dependence in the electron lifetimes, which has been discussed for the storm main phases. During the prestorm intervals, the energy dependence index α was consistently negative for the two nonmajor storms in the solar minimum (higher energy electrons lost faster) with lifetimes generally greater than 10 days (see Figures 5 and 7). However, for the intense storm the sign of α was positive at the peak electron flux location in the quiet interval before the storm (first column in Figure 9), and with lifetimes within the range of 1–10 days, shorter than the other two less intense storms. In some intervals of the storm recovery phases, when the electron lifetimes were still shorter than the prestorm levels, the sign of the energy dependence index basically remained the same with the storm main phases (being negative). This makes sense if the same loss mechanism was still active during those periods. However, when the electron lifetimes increased back to the prestorm values in the recovery phases, indicating slow loss processes for all energy electrons considered here, the sign of energy dependence could turn out to be reversed compared to the quiet interval before the storm (e.g., L = 3.5 in the September 2002 storm and L = 5.5 in February 2009 storm). Therefore, based on our results, we

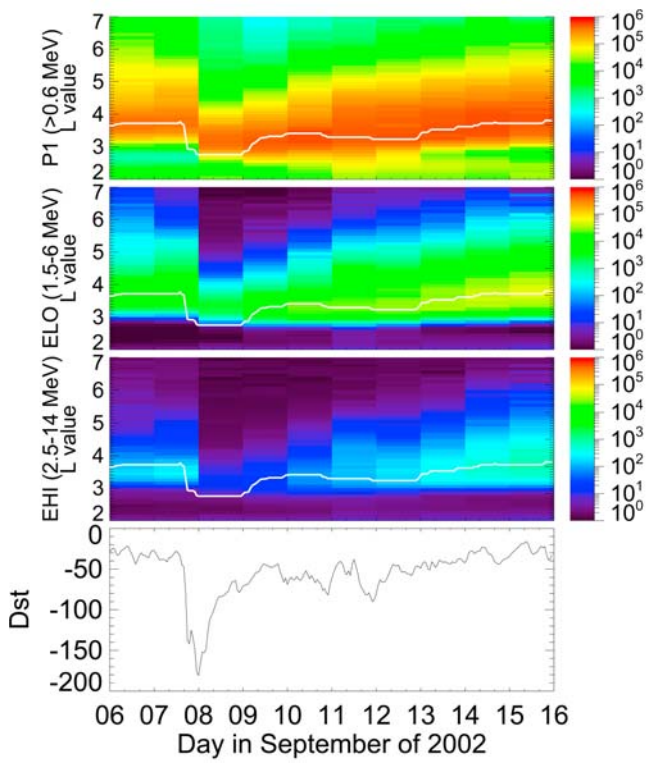

Figure 8. Electron count rate variations and Dst profile over the September 2002 storm. The configuration is the same with Figures 3 and 6, but with the L ranges for the Y axes in the top three panels broadened to L = 2–7.

can conclude that the energy dependence in the electron lifetimes can vary with storms, with time during a storm, and with locations.

[38] Another property to look into is the local time dependence of the electron loss rate. As we mentioned, for the February 2009 storm significant dawn/dusk asymmetry of the pitch angle diffusion rates occurred during the storm main phase at L = 5.5, with diffusion at dawn ~2000 times faster than that at dusk. To illustrate the strong LT dependence, the electron count rate data and three different model simulations for that time period (DOY 45.3–45.8 of 2009) at L = 5.5 were shown in Figure 10, with the pattern similar to Figure 4. So Figures 10a–10c illustrate the same count rate data (filled triangles) but different simulation results (open triangles). The number indices are similar to those in Figure 2b, which number the 33 crossings at L = 5.5 within this half a day in chronological order, but with the dawnside crossings in red indices and the duskside crossings in black, so that we can clearly distinguish the dawnside and duskside measurements. By looking at the data (filled triangles), we noticed the dawnside crossings (with red indices, basically on the right-hand side of each panel) generally have high count rates, which were almost on the same level with the trapped electron rates (green triangles), indicating a very fast pitch angle diffusion rate at dawn; while the duskside rates (with black indices, on the left-hand side) were very low, suggesting a slow diffusion there. Therefore, to simulate the count rates within this interval requires a strong dawn/dusk asymmetry.

[39] Our model, with separate and values, is capable of resolving the LT dependence in D_{xx}. Figure 10a shows the best fit results from our model, simulating the entire count rate versus longitude distribution and the separation of the dawn/dusk count rates reasonably well, with D_{dawn} = $10^{-6.022}$ s^{-1}, $D_{dusk} = 10^{-9.399}$ s^{-1}, and the model performance index K^2 = 0.23. So D_{dawn}/D_{dusk} = 2382, with diffusion at dawn much faster than at dusk. To further support our results, we performed some test runs for this time interval without LT asymmetry. D_{dawn} was forced to be equal to D_{dusk}, with the case when PA diffusion at dawn and dusk were both fast in Figure 10b ($D_{dawn} = D_{dusk} = 10^{-6.022}$ s^{-1}) and the case with diffusion both slow in Figure 10c ($D_{dawn} = D_{dusk} = 10^{-9.399}$ s^{-1}). Compared with the results in Figure 10a, for the Figure 10b case the duskside count rates were generally over-reproduced by the model; while the dawnside count rate data were underreproduced due to the insufficient simulations of the trapped electrons (green triangles). The K^2 for this case was ~0.37. However, for the case with slow diffusion at both dawn and dusk (Figure 10c), the trapped electrons were greatly overestimated and the entire count rate distribution was poorly simulated (K^2 = 0.53). Therefore, strong dawn/dusk asymmetry in D_{xx} is definitely necessary to model this interval.

[40] Furthermore, by investigating the specific LT coverage of the SAMPEX crossings during this time period, we found that the observed fast pitch angle diffusion (with electron lifetimes on the order of hours) mainly occurred at ~08 h LT. Even though we cannot rule out possible fast diffusion at other LT regions not covered by SAMPEX for this case, based on the distinct and values for the model results shown in Figure 10a, it was confirmed that pitch angle diffusion, on average, was much faster at dawn than at dusk during the main phase of this storm at L = 5.5.

[41] Strong dawn/dusk asymmetry in the pitch angle diffusion rate was also found for the September 2002 storm (the most intense storm). But it appeared in the early recovery phase (the first day in the recovery phase) and at L = 3.5 (peak flux location), with dusk side 100 times faster than dawn. One thing to note is that during this early recovery phase, the electron lifetime was still short (~0.1 day, comparable to the lifetimes during main phase). For March 2008 storm, considerable dawn/dusk asymmetry showed up also during the early recovery phase (when the lifetime was also shorter than the quiet prestorm level, but in this case not comparable to the main phase values, but ≥10 times longer), and over a wide L range (L = 4.5 to L = 6.5), with dawn faster than dusk by 10–100 times. Those are the most significant local time variances of electron loss rates from our results, yet with very little local time dependence observed at other locations or during other storm phases.

[42] The above are the primary characteristics of the electron lifetimes inferred from our model results. These features must be related to the changes in the scattering mechanisms, the wave spectra, and the plasma properties, the detailed analysis of which is yet beyond the scope of this paper. But the merit of our model is that using SAMPEX observation we can provide quantitative results on these detailed properties of the electron loss rates, which will lay the basis for the specific wave loss mechanism studies.

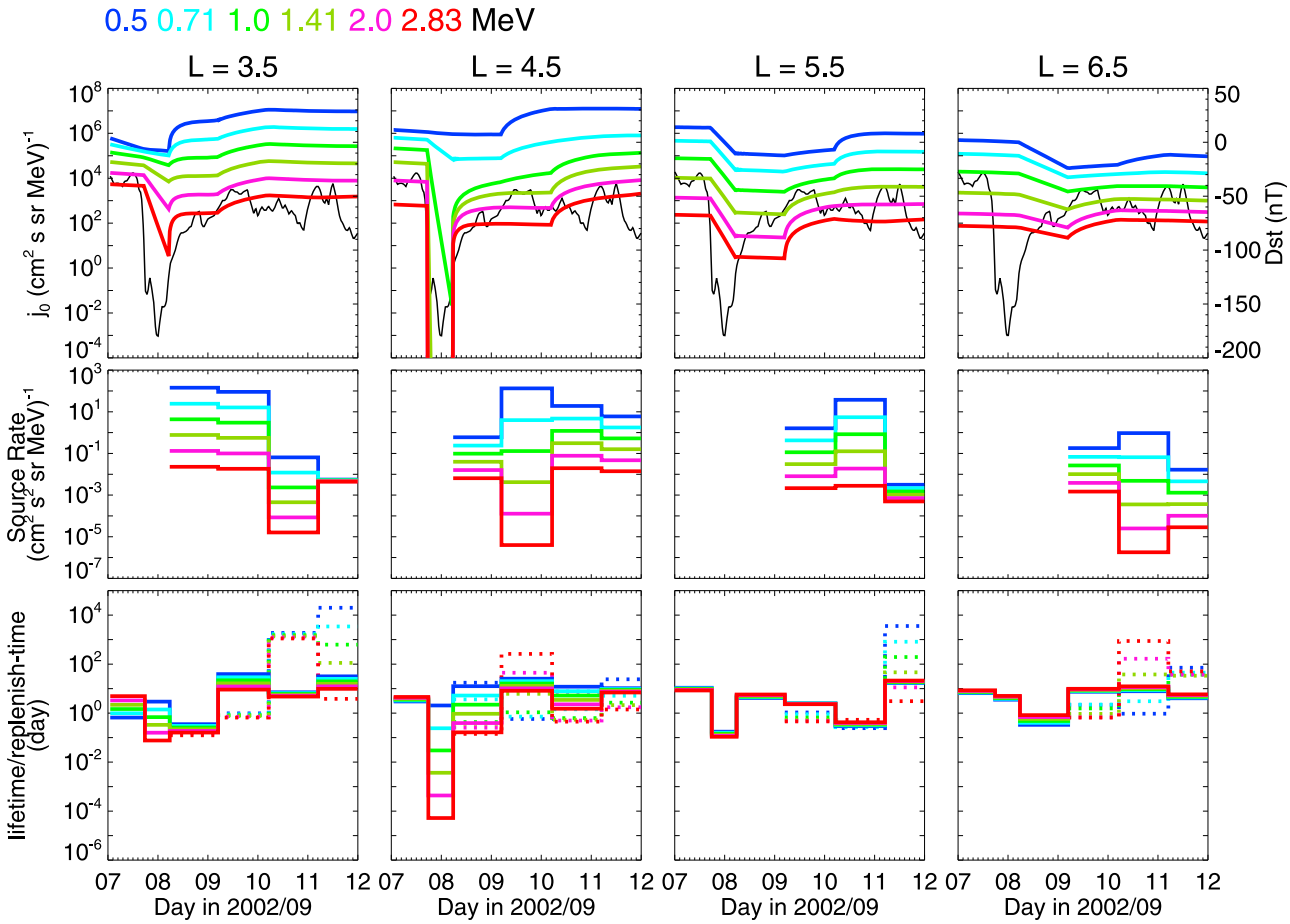

Figure 9. Model results for the September 2002 storm at different L. The configuration is the same with Figures 5 and 7.

5.3. Source Mechanisms

[43] As we introduced, the estimated source rate from our model is comprehensive, including both radial diffusion and local heating. Can we separate them? For radial diffusion, the peak of electron phase space density (PSD) is at the outer boundary (higher L region) and the PSD gradient is positive throughout. So the electrons diffuse inward from the outer boundary and get energized. On the other hand, for in situ acceleration, there is an internal peak for PSD and the electrons can diffusion both inward and outward. For the estimated source rate, to quantitatively determine the relative contributions from radial diffusion and from local acceleration needs a more complicated model that explicitly includes the radial diffusion term, which will turn the 2-D model to 3-D.

[44] But since here we have run the 2-D model for a range of L values, is it possible to at least qualitatively disentangle radial diffusion from local heating by investigating the evolution of source rates at different L regions? It is still not easy considering the time length of each data interval, mostly daily during the recovery phase. Since within a day the MeV electrons can drift many times around the earth, if radial diffusion occurs, it is possible to see sources in all L for that interval. On the other hand, if local heating is active at some L region, within a day it can also diffuse to other L regions. Therefore, generally speaking, the variation time scale of the source rate in the current model is not enough to resolve the different evolutions of radial diffusion and internal heating. This is the case for the results of February 2009 and March 2008 storms. However, for September 2002 storm with results shown in Figure 9, we noticed that during the early recovery phase (first day in the recovery phase), source was active only locally in L = 3.5 and 4.5 but not in L = 5.5 and 6.5. But later in the recovery phase, active source appeared at all L regions. Therefore, it is possible that during the early recovery phase local heating occurred at around L = 3.5–4.5, and meanwhile, radial diffusion was too slow to transport electrons to other L regions. Later on, if the source rate at higher L (L = 5.5–6.5) was due to outward diffusion from the internal source at L = 3.5–4.5 or due to inward diffusion from some other external sources is still uncertain.

5.4. Parameter Sensitivity

[45] We can investigate the parameter sensitivity of our model by calculating the change in the model metric K^2 (defined in equation (4)) in response to a given fractional change (here as ±20%) in each of the free parameters (D_{dawn}, D_{dusk} and α in the diffusion term (equation (2)), and S_0 and ν in the source term (equation (3))). The February 2009 event run at L = 4.5 (Figure 4) was selected for the

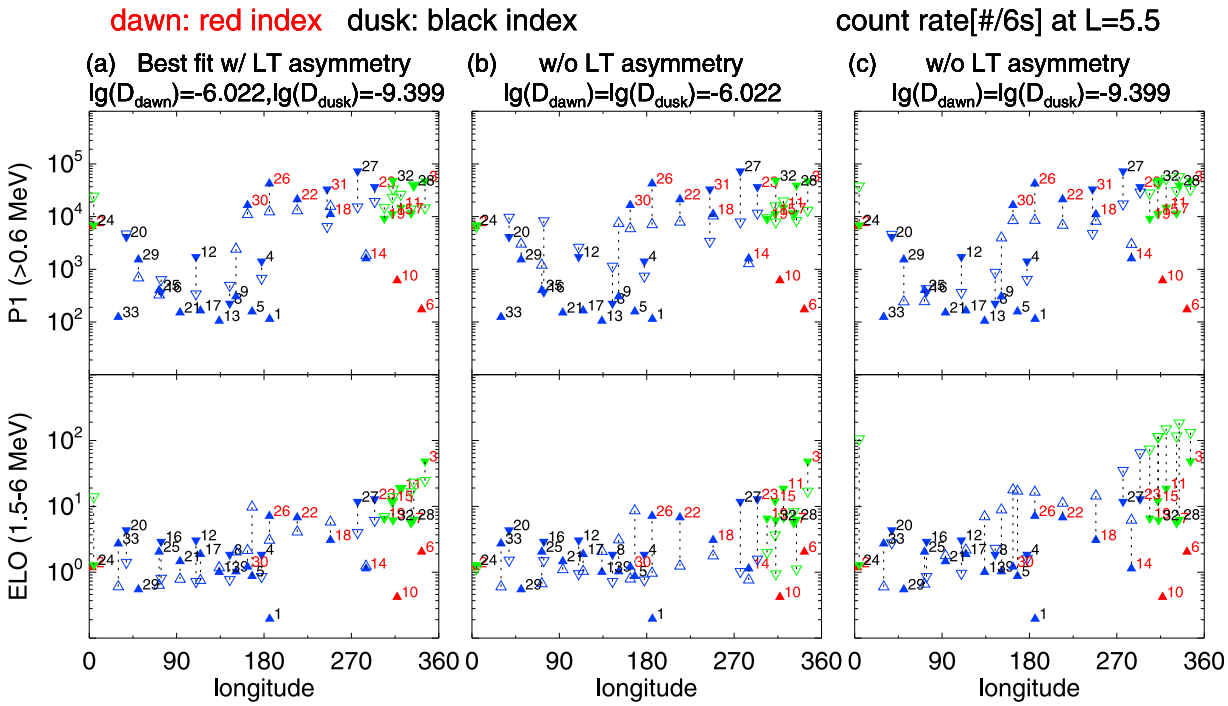

Figure 10. Electron count rate data (filled triangles) and three model simulations (open triangles) for counters P1 and ELO at $L = 5.5$ during the storm main phase of February 2009 storm. The pattern is similar to Figure 4 except for the number indices, which number the 33 crossings at $L = 5.5$ within this half a day in chronological order, with the crossings in dawn in red indices and the crossings in dusk in black. Figure 10a shows the best-fit simulation from the model with dawn/dusk asymmetry ($\lg(D_{dawn}) = -6.022$ and $\lg(D_{dusk}) = -9.399$), compared with the simulations without dawn/dusk asymmetry, $\lg(D_{dawn}) = \lg(D_{dusk}) = -6.022$ in Figure 10b and $\lg(D_{dawn}) = \lg(D_{dusk}) = -9.399$ in Figure 10c.

sensitivity study. We found that when pitch angle diffusion was strong the model performed very sensitive to the diffusion-related parameters. For example, during the main phase of February 2009 storm (Figure 4b), K^2 could change by ~10% with respect to the 20% change in D_{dawn}, and $D_{dawn/dusk}$ turned out to be more sensitive parameters than the energy dependence index α. However, when pitch angle diffusion became slow and the source term turned more significant during the storm recovery phase (Figures 4c–4f), the model was more sensitive to the source term-related parameters and much less sensitive to the parameters in the diffusion term. For example, the values of K^2 could change by >20% for the 20% change in ν, the energy dependence index in source, but vary only within 1% for the same fractional changes in all the diffusion term parameters.

5.5. Model Limitations and Error Sources

[46] Now we discuss the model limitations and some possible sources of error involved in the model and the simulation results. First, our model uses some simplified assumptions, such as the uniform exponential energy dependence in D_{xx} (equation (2)) and S (equation (3)) and the fixed power index 30 on x in D_{xx}. Although these parameterized forms of D_{xx} and S could differ from the estimations from the quasi-linear wave study [e.g., *Li et al.*, 2007], which are also accompanied with uncertainties, the good performance of our model both in this paper and in the paper of *Selesnick* [2006] proves that the forms of D_{xx} and S used in the model are generally reasonable. Second, as previously discussed, when the loss of the electrons is so fast that it approaches the strong diffusion limit, the current model is not accurate in determining the specific electron loss rates.

5.5.1. At High Electron Energies

[47] Large uncertainties of the model results at high energies may occur when the electron count rate data from detector ELO and EHI are significantly low (close to the data background levels) and the energy dependence in D_{xx} represented by equation (2) is relatively strong (specifically, with $\alpha < -2$ from model experiments). Among all the model results shown in the paper there are two such cases: the main phase results at $L = 5.5$ for February 2009 storm and at $L = 4.5$ for September 2002 storm. Under this situation, the energy dependence index α is primarily determined by the low-energy data (or responses of PET detectors at low-energy range). Then the very low fluxes and short electron lifetimes at high energies are not well constrained by the data but directly derived from the uniform exponential energy dependence in equation (2). In other words, the limitation from the energy dependence form in D_{xx} leads to the model inaccuracy at high energies. Therefore, for the two cases mentioned above there are uncertainties in the model results at high energy levels: specifically, in Figure 5 the much lower trapped flux j_0 and much shorter electron lifetimes of $E \geq 2$ MeV electrons at $L = 5.5$ than at other L during the main phase of February 2009 storm; and similarly in Figure 9 the very low j_0 and short lifetimes at $L = 4.5$ at $E \geq 1.41$ MeV during the September 2002 storm main phase. The lower threshold of the less-constrained model energy range for each

case (e.g., 2 MeV for the first case and 1.41 MeV for the second) is determined by a sensitivity study (changing the model flux at the highest energy to zero to see if the simulated data change; if not, try the second highest energy, etc.).

5.5.2. At High *L* Regions

[48] Additional attention must be paid to the estimated loss rates for high L shell regions, where magnetopause shadowing and outward radial diffusion, other electron loss mechanisms besides pitch angle diffusion, can be significant. In that case, the estimated loss rate would not be accurate but as an approximation of the overall loss. As to the quantitative estimate of the other two loss mechanisms a more complicated model that explicitly includes radial diffusion terms is needed. Another problem at high L lies in the L value calculation. The L values used in this study were obtained from the SAMPEX data, which are calculated based on the IGRF model. But during geomagnetically active times, such as the September 2002 storm here, the external field from magnetospheric currents can be important, bringing errors into the L calculation. For these reasons, we have compared the L values directly from the data and those calculated using the Tsyganenko 2001 storm model (T01S) parameterized by solar wind and geomagnetic indices, which is considered reasonably accurate at low altitude. The comparison showed that inside $L = 6$ the IGRF L values from the data are quantitatively comparable to the T01S L values. Deviations are more obvious beyond $L = 6$. But since during intense storms, the region inside $L = 6$ is considered the more active region for electron precipitation where the electron count rate data were higher and showed more dynamics, using the L values from the IGRF model is still fine for our main results.

[49] Based on the limitation discussed above, it would be interesting to examine the loss rate results for $L = 5.5$ and 6.5 in the September 2002 storm, which are generally energy independent. We calculated the last closed drift shell during this intense storm and found it could be as low as $L^* = 5.3$ for electrons with 90° equatorial PA during the storm main phase (L^* here is Roederer L [*Roederer*, 1970] calculated using Tsyganenko 2001 storm model). So could it be magnetopause shadowing that caused the energy-independent losses at $L = 5.5$ and 6.5 during the storm main and early recovery phases? The speculation was not supported by the fact that there was no sudden depletion of the trapped electron flux (j_0) at $L = 5.5$ and 6.5 during the storm main phase (the first row of Figure 9). Considering the errors in L values discussed above and that the last closed drift shell is PA dependent (the data we modeled are centered around DLC), $L = 5.5$ and 6.5 in our model could still be closed drift shells even though the last closed drift shell for equatorially mirroring electrons is at $L^* = 5.3$. So the loss mechanism at $L = 5.5$ and 6.5 other than pitch angle scattering was more likely to be outward radial diffusion rather than direct magnetopause shadowing. And again, due to the errors in L calculation for high L regions and the fact that the count rates there were very low with more statistical errors, the results for September 2002 storm at $L = 5.5$ and 6.5 could have more uncertainties.

5.5.3. At High Equatorial Pitch Angles

[50] The model works to simulate the whole pitch angle distribution although the data constraints from SAMPEX only cover low equatorial PA range around the loss cone angles. To constrain the model results at high equatorial PA, high-altitude data covering larger equatorial PA could be used, as carried out in the study of *Selesnick et al.* [2003]. We agree it would be a plus for this work if our model results are also compared against observations at higher altitude. But it was not performed here since the focus in this work is the electron loss rate, for which using the low-altitude data from SAMPEX is adequate. This is because the SAMPEX data already well cover the BLC, DLC, and some trapped-electron PA, and based on previous simulation work we know that if the PA distribution reaches an equilibrium shape the electron loss rate is primarily controlled by the minimum PA diffusion rate [*Albert and Shprits*, 2009], near the edge of the loss cone here. Therefore, even without the constraints on model results with high equatorial PA, the estimated electron loss rates from our model are still reliable. However, the quantified electron source rates will have fewer uncertainties for the PA ranges covered by SAMPEX, more uncertainties at higher equatorial PA close to 90°.

5.5.4. Adiabatic Corrections

[51] In this work, we did not perform the adiabatic corrections on the model results. It was shown previously [*Selesnick*, 2006] that for low-altitude electron data, the most significant adiabatic effects are the changes in mirror point altitudes and the associated energy changes during intense storms. The adiabatic intensity change observed by SAMPEX due to the raise of the mirror point can be quickly compensated by even moderate pitch angle diffusion. And by investigating if the DLC is empty, we can easily determine whether such diffusion has occurred.

[52] *Selesnick* [2006] proved that the adiabatic effects were small for low-altitude electrons based on the model results for two intense storms, although only for a small $L = 3.5$. But as previously discussed, during the intense storm the results on the higher L regions already have larger errors and need to be taken with caution. And in the main phases of our studied storm events, the quasi-trapped electron intensities in the DLC were generally higher than the BLC electrons, except for the fast loss case at $L = 4.5$ during the main phase of September 2002 storm, when the DLC and BLC contents were comparably low. Would the fast losses be a result of adiabatic changes? The estimated fast loss time scale was on the order of minutes, comparable to the electron drift period, and the fast loss only occurred at $L = 4.5$, rather than a wide L region as expected from adiabatic effects. Therefore, the fast loss was a nonadiabatic process, and generally, the adiabatic effects are insignificant in our work.

[53] Another limitation of the current model is that it cannot resolve the variations of the electron loss rates on time scales shorter than 12 h, which is constrained by the length of time required for the data to reach full longitude coverage. This is currently the best we can get out of the available data. Even though the model parameter values varied rapidly between intervals, the changes of model intensities were still gradual (as seen in, e.g., first row of Figure 9), as it took time for the model to respond to the new set of parameters. Additionally, due to the nature of electron lifetime (only defined for an equilibrium state as discussed in section 3), the estimated electron lifetime merely represents an average loss over each modeled period (1/2 day to a day), which indicates the possibility that sometime during that interval the instant electron

loss rate can be actually higher, e.g., faster than hours for February 2009 storm main phase.

5.6. Merits of Our Method for Electron Lifetime Quantification

[54] As discussed in the beginning of this paper, the uncertainties and difficulties in the theoretical precipitation loss studies have guided researchers to use the empirical forms of electron loss rates (e.g., depending on the geomagnetic indices), which are erratic and can differ by an order of magnitude. Our method, directly comparing the drift diffusion model results with the low-altitude electron data, is capable of providing more reliable results on the quantification of electron loss rate, as well as its temporal and spatial variations, as shown in Figures 5, 7, and 9. The results from this work can be applied to, e.g., the particle tracing codes, the radial diffusion codes, and the comprehensive radiation belt dynamics models.

[55] It is also interesting to compare the quantification results of the electron loss rates from our model approach to some results from the theoretical quasi-linear wave study approach. *Summers et al.* [2007] performed comprehensive study on the theoretical quasi-linear pitch angle diffusion rates of the outer zone radiation belt electrons, due to the scattering by chorus, plasmaspheric hiss, and EMIC waves, separately and in combination. They made certain assumptions on the wave and plasma properties and then the bounce-averaged pitch angle diffusion coefficients and corresponding electron loss time scales were evaluated. They found that the precipitation loss time scales of electrons due to resonant pitch angle diffusion by each of the wave modes, chorus, hiss, and EMIC waves, can be 1 day or less, and are also energy and L dependent.

[56] Specifically, the results on the electron precipitation by plasmaspheric hiss showed that during low geomagnetic activity times and for electrons with energy exceeding 500 keV, the loss time scales over the range $3 \leq L \leq 5$ are between 1 and 10 days, with higher energy electrons lost slightly slower. This is generally consistent with our electron lifetime results at the quiet interval before the September 2002 storm for electrons with similar energy range and at similar L locations (see Figure 9). *Summers et al.* [2007] also suggested that the electron loss time scales due to EMIC wave scattering, over the energy range 0.9–5 MeV and at $L = 3$–5, are on the order of hours, decreasing as L gets larger, and with faster loss at higher energies. We also see the similar features in our main phase electron lifetimes at $L = 3.5$ and $L = 4.5$ for September 2002 storm and at $L = 4.5$ for the other two storms.

[57] As described above, we can always try to match our model results to the theoretical wave study results aiming at revealing the primary wave mode that causing the electron loss. However, without comprehensive observational data on the spectral properties of these waves and on the other assumed factors in the theoretical study listed above, the theoretical quasi-linear wave approach is not able to accurately determine the electron loss rate and its variations, and those observations are beyond our current capabilities. On the other hand, our model approach combined with the low-altitude electron data can directly quantify the simultaneous electron loss rates, not requiring detailed information on the above factors, which is another advantage of our method. Therefore, it will be useful to turn the other way around and refer to the quantitative electron loss rate results from our model approach in the theoretical wave loss studies.

6. Summary and Conclusions

[58] In this paper, the rates and the spatial and temporal variations of electron precipitation loss to the atmosphere in the Earth's radiation belt were studied. Since the electron bounce loss cone opens up at low altitude, the low-altitude electron measurements are the most useful in determining the electron precipitation loss rate into the atmosphere, of which we used the SAMPEX/PET electron count rate data. A drift diffusion model was inherited from previous work to simulate the low-altitude electron distribution observed by SAMPEX as a delicate balance of azimuthal drift, pitch angle diffusion into the upper atmosphere, and possible concurrent sources. After pursuing the best fit of the modeled electron rates to the data within each time interval (1 day or half a day), the optimum sets of parameter values were obtained, based on which the magnitudes and variations of the electron lifetime can be quantitatively determined.

[59] Three magnetic storms that fall into different categories of storm magnitude were selected for detailed event study, including a small storm and a moderate storm within the current deep solar minimum and an intense storm right after the last solar maximum. The loss rates for electrons with energy from ~0.5 to 3 MeV were estimated at L regions from $L = 3.5$ to $L = 6.5$ over different phases of the three individual storm events. One common feature of the electron lifetimes was discovered based on our model results, that during the storm main phases of all the three events, fast precipitation losses of energetic radiation belt electrons, as short as hours, persistently occurred over wide range of L regions and over all the local times covered by SAMPEX, and with faster loss for higher energy electrons. The underlying electron loss mechanisms remain an open question, but the results strongly indicated that there must be some quick scattering processes, functioning preferably on higher energy electrons. Some other properties of the electron loss rates were also investigated in this work. Model results over different phases of the three individual events and at various L locations suggested that the energy dependence in the electron lifetimes differed for different storms, and could be time dependent and L dependent. And significant dawn/dusk asymmetry in the electron loss rate can show up during the storm main phase or recovery phase in different storms, with the pitch angle diffusion rate at dawn faster than at dusk or vice versa, but primarily around the peak electron flux locations.

[60] The method used in this work, combining the low-altitude observations with the drift diffusion model, is capable of providing direct quantification of the electron loss rate, which is a required step towards developing comprehensive models for the radiation belt electron dynamics, and is capable of determining the spatial and temporal variations of the electron precipitation loss into the atmosphere, useful for the theoretical wave-particle interaction studies aiming for the essential loss mechanisms.

[61] **Acknowledgments.** The work was supported by NASA grant (NNX09AJ57G), NSF grant (ATM-0842388), and also by grants from the National Natural Science Foundation of China (40621003 and 40728005).

[62] Zuyin Pu thanks Jay Albert Yue Chen for their assistance in evaluating this paper.

References

Albert, J. M. (2003), Evaluation of quasi-linear diffusion coefficients for EMIC waves in a multispecies plasma, *J. Geophys. Res.*, *108*(A6), 1249, doi:10.1029/2002JA009792.

Albert, J. M., and Y. Y. Shprits (2009), Estimates of lifetimes against pitch angle diffusion, *J. Atmos. Sol.-Terr. Phys.*, *71*, 1647–1652, doi:10.1016/j.jastp.2008.07.004.

Baker, D. N., et al. (1993), An overview of the SAMPEX mission, *IEEE Trans. Geosci. Remote Sens.*, *31*, 531, 1993.

Barker, A. B., X. Li, and R. S. Selesnick (2005), Modeling the radiation belt electrons with radial diffusion driven by the solar wind, *Space Weather*, *3*, S10003, doi:10.1029/2004SW000118.

Chen, Y., et al. (2007), The Energization of Relativistic Electrons in the Outer Van Allen Radiation Belt, *Nature*, *3*(9), 614–617, doi:10.1038/nphys655.

Cook, W. R., et al. (1993), PET: A Proton/Electron Telescope for studies of magnetospheric, solar, and galactic particles, *IEEE Trans. Geosci. Remote Sens.*, *31*, 565–571.

Elkington, S. R., M. K. Hudson, and A. A. Chan (2003), Resonant acceleration and diffusion of outer zone electrons in an asymmetric geomagnetic field, *J. Geophys. Res.*, *108*(A3), 1116, doi:10.1029/2001JA009202.

Engebretson, M. J., et al. (2008), Pc1–Pc2 waves and energetic particle precipitation during and after magnetic storms: Superposed epoch analysis and case studies, *J. Geophys. Res.*, *113*(A1), A01211, doi:10.1029/2007JA012362.

Erlandson, R. E., and A. J. Ukhorskiy (2001), Observations of electromagnetic ion cyclotron waves during geomagnetic storms: Wave occurrence and pitch angle scattering, *J. Geophys. Res.*, *106*(A3), 3883–3895.

Friedel, R. H. W., G. Reevesa, and T. Obara (2002), Relativistic electron dynamics in the inner magnetosphere – a review, *J. Atmos. Sol.-Terr. Phys.*, *64*, 265–282.

Gustafsson, G., N. E. Papitashvili, and V. O. Papitashvili (1992), A Revised Corrected Geomagnetic Coordinate System for Epochs 1985 and 1990, *J. Atmos. Sol.-Terr. Phys.*, *54*, 1609–1631.

Kennel, C. F., and H. E. Petschek (1966), Limit on stably trapped particle fluxes, *J. Geophys. Res.*, *71*(1), 1–27.

Li, W., Y. Y. Shprits, and R. M. Thorne (2007), Dynamic evolution of energetic outer zone electrons due to wave-particle interactions during storms, *J. Geophys. Res.*, *112*(A10), A10220, doi:10.1029/2007JA012368.

Li, X. (2004), Variations of 0.7–6.0 MeV electrons at geosynchronous orbit as a function of solar wind, *Space Weather*, *2*, S03006, doi:10.1029/2003SW000017.

Li, X., et al. (1997), Multisatellite observations of the outer zone electron variation during the November 3–4, 1993, magnetic storm, *J. Geophys. Res.*, *102*(A7), 14,123–14,140.

Mabry, D. J., S. J. Hansel, and J. B. Blake (1993), The SAMPEX data Processing Unit (DPU). *IEEE Trans. Geosci. Remote Sens.*, *31*, 572–574.

McIlwain, C. E. (1961), Coordinates for mapping the distribution of magnetically trapped particles, *J. Geophys. Res.*, *66*(11), 3681–3691.

Meredith, N. P., et al. (2003), Statistical analysis of relativistic electron energies for cyclotron resonance with EMIC waves observed on CRRES, *J. Geophys. Res.*, *108*(A6), 1250, doi:10.1029/2002JA009700.

Mewaldt, R. A., et al. (2005), Proton, helium, and electron spectra during the large solar particle events of October–November 2003, *J. Geophys. Res.*, *110*(A9), A09S18, doi:10.1029/2005JA011038.

Millan, R. M., and R. M. Thorne (2007), Review of radiation belt relativistic electron loss, *J. Atmos. Sol.-Terr. Phys.*, *69*, 363–377.

O'Brien, T. P., and M. B. Moldwin (2003), Empirical plasmapause models from magnetic indices, *Geophys. Res. Lett.*, *30*(4), 1152, doi:10.1029/2002GL016007.

Reeves, G. D., et al. (2003), Acceleration and loss of relativistic electrons during geomagnetic storms, *Geophys. Res. Lett.*, *30*(10), 1529, doi:10.1029/2002GL016513.

Roederer, J. G. (1970), *Dynamics of Geomagnetically Trapped Radiation*, Springer-Verlag Berlin, New York, *Physics and Chemistry in Space*, *2*, 166 pp.

Schulz, M., and L. Lanzerotti (1974), *Particle Diffusion in the Radiation Belts*, Springer, New York.

Selesnick, R. S. (2006), Source and loss rates of radiation belt relativistic electrons during magnetic storms, *J. Geophys. Res.*, *111*(A4), A04210, doi:10.1029/2005JA011473.

Selesnick, R. S., and J. B. Blake (2000), On the source location of radiation belt relativistic electrons, *J. Geophys. Res.*, *105*(A2), 2607–2624, doi:10.1029/1999JA900445.

Selesnick, R. S., J. B. Blake, and R. A. Mewaldt (2003), Atmospheric losses of radiation belt electrons, *J. Geophys. Res.*, *108*(A12), 1468, doi:10.1029/2003JA010160.

Selesnick, R. S., M. D. Looper, and J. M. Albert (2004), Low-altitude distribution of radiation belt electrons, *J. Geophys. Res.*, *109*(A11), A11209, doi:10.1029/2004JA010611.

Shprits, Y. Y., and R. M. Thorne (2004), Time dependent radial diffusion modeling of relativistic electrons with realistic loss rates, *Geophys. Res. Lett.*, *31*(8), L08805, doi:10.1029/2004GL019591.

Shprits, Y. Y., et al. (2005), Radial diffusion modeling with empirical lifetimes: Comparison with CRRES observations, *Ann. Geophys.*, *23*, 1467–1471.

Shprits, Y. Y., et al. (2006), Outward radial diffusion driven by losses at magnetopause, *J. Geophys. Res.*, *111*(A11), A11214, doi:10.1029/2006JA011657.

Shprits, Y. Y., N. P. Meredith, and R. M. Thorne (2007), Parameterization of radiation belt electron loss timescales due to interactions with chorus waves, *Geophys. Res. Lett.*, *34*(11), L11110, doi:10.1029/2006GL029050.

Summers, D., and R. M. Thorne (2003), Relativistic electron pitch-angle scattering by electromagnetic ion cyclotron waves during geomagnetic storms, *J. Geophys. Res.*, *108*(A4), 1143, doi:10.1029/2002JA009489.

Summers, D., R. M. Thorne, and F. Xiao (1998), Relativistic theory of wave-particle resonant diffusion with application to electron acceleration in the magnetosphere, *J. Geophys. Res.*, *103*(A9), 20,487–20,500.

Summers, D., B. Ni, and N. P. Meredith (2007), Timescales for radiation belt electron acceleration and loss due to resonant wave-particle interactions: 2. Evaluation for VLF chorus, ELF hiss, and electromagnetic ion cyclotron waves, *J. Geophys. Res.*, *112*(A4), A04207, doi:10.1029/2006JA011993.

Tarantola, A. (2005), *Inverse Problem Theory and Methods for Model Parameter Estimation*, Society for Industrial and Applied Mathematics, ISBN 0-89871-572-5.

Thorne, R. M., and C. F. Kennel (1971), Relativistic electron precipitation during magnetic storm main phase, *J. Geophys. Res.*, *76*(19), 4446–4453.

Thorne, R. M., et al. (2005), Timescale for MeV electron microburst loss during geomagnetic storms, *J. Geophys. Res.*, *110*(A9), A09202, doi:10.1029/2004JA010882.

Tu, W., et al. (2009), Storm-dependent radiation belt electron dynamics, *J. Geophys. Res.*, *114*(A2), A02217, doi:10.1029/2008JA013480.

Ukhorskiy, A. Y., et al. (2005), Impact of toroidal ULF waves on the outer radiation belt electrons, *J. Geophys. Res.*, *110*(A10), A10202, doi:10.1029/2005JA011017.

X. Li, Laboratory for Space Weather, Chinese Academy of Sciences, 52 Sanlihe Rd., Beijing 100864, China.

M. Looper, Space Sciences Department, The Aerospace Corporation, PO Box 92957, Los Angeles, CA 90009-2957, USA.

W. Tu, LASP and Department of Aerospace Engineering Sciences, University of Colorado at Boulder, 1234 Innovation Dr., Boulder, CO 80303, USA. (tu@colorado.edu)